

PAPER

Nanofluidic crystal: a facile, high-efficiency and high-power-density scaling up scheme for energy harvesting based on nanofluidic reverse electrodialysis

To cite this article: Wei Ouyang *et al* 2013 *Nanotechnology* **24** 345401

View the [article online](#) for updates and enhancements.

You may also like

- [Nanofluidic charged-coupled devices for controlled DNA transport and separation](#)
Reza Nouri and Weihua Guan
- [Voltage gated ion and molecule transport in engineered nanochannels: theory, fabrication and applications](#)
Weihua Guan, Sylvia Xin Li and Mark A Reed
- [Carbon nanostructure based mechano-nanofluidics](#)
Wei Cao, Jin Wang and Ming Ma



HONOLULU, HI
Oct 6–11, 2024

Abstract submission deadline:
April 12, 2024

Learn more and submit!



Joint Meeting of

The Electrochemical Society
•
The Electrochemical Society of Japan
•
Korea Electrochemical Society

Nanofluidic crystal: a facile, high-efficiency and high-power-density scaling up scheme for energy harvesting based on nanofluidic reverse electrodialysis

Wei Ouyang¹, Wei Wang^{1,2}, Haixia Zhang^{1,2}, Wengang Wu^{1,2} and Zhihong Li^{1,2}

¹ Institute of Microelectronics, Peking University, Beijing 100871, People's Republic of China

² National Key Laboratory of Science and Technology on Micro/Nano Fabrication, Beijing 100871, People's Republic of China

E-mail: w.wang@pku.edu.cn


Received 12 April 2013, in final form 9 July 2013

Published 30 July 2013

Online at stacks.iop.org/Nano/24/345401

Abstract

The great advances in nanotechnology call for advances in miniaturized power sources for micro/nano-scale systems. Nanofluidic channels have received great attention as promising high-power-density substitutes for ion exchange membranes for use in energy harvesting from ambient ionic concentration gradient, namely reverse electrodialysis. This paper proposes the nanofluidic crystal (NFC), of packed nanoparticles in micro-meter-sized confined space, as a facile, high-efficiency and high-power-density scaling-up scheme for energy harvesting by nanofluidic reverse electrodialysis (NRED). Obtained from the self-assembly of nanoparticles in a micropore, the NFC forms an ion-selective network with enormous nanochannels due to electrical double-layer overlap in the nanoparticle interstices. As a proof-of-concept demonstration, a maximum efficiency of $42.3 \pm 1.84\%$, a maximum power density of $2.82 \pm 0.22 \text{ W m}^{-2}$, and a maximum output power of $1.17 \pm 0.09 \text{ nW/unit}$ (nearly three orders of magnitude of amplification compared to other NREDs) were achieved in our prototype cell, which was prepared within 30 min. The current NFC-based prototype cell can be parallelized and cascaded to achieve the desired output power and open circuit voltage. This NFC-based scaling-up scheme for energy harvesting based on NRED is promising for the building of self-powered micro/nano-scale systems.

 Online supplementary data available from stacks.iop.org/Nano/24/345401/mmedia

(Some figures may appear in colour only in the online journal)

1. Introduction

With the development of nanotechnology, there is an ever-growing demand for miniaturized power sources for micro/nano-scale systems, such as in remote environmental sensors, implantable biosensors and biomedical devices.

Micro/nano-scale systems usually operate at low power levels ranging from nanowatts to microwatts [1], making it possible to build self-powered systems by harvesting energy from ambient. Apart from the extensively studied solar energy [2], thermal energy [3], and vibration energy [4], the Gibbs free energy can also be converted into electricity

by so-called reverse electrodialysis (RED), by establishing an ionic concentration gradient which is widely existent in nature or in human body across ion-selective membranes. This concept was proposed by Pattle *et al* [5] in 1954 and has been extensively studied since then in large-scale ion exchange membrane (IEM) based RED systems by the mixing of sea and river water [6–11]. For example, Veerman *et al* [10] obtained a power density of 0.93 W m^{-2} in an optimized cell with 50 IEM pairs, and Vermaas *et al* [11] achieved a power density of 1.2 W m^{-2} using a stack of 5 IEM pairs with an inter-membrane distance of $100 \mu\text{m}$. A theoretical maximum power density of 2.7 W m^{-2} has been predicted using parameters typical for the current state of technology [12]. In recent years, miniaturized IEM-based RED systems have also attracted research interest. A miniaturized IEM-based concentration cell was realized with a power density of 0.2 mW m^{-2} and efficiency of 0.44% by Sadeghian *et al* [13]. Sales *et al* [14] obtained a maximum peak power density of 72 mW m^{-2} together with a maximum efficiency of 22% in a flow cell combining IEMs and porous electrodes. The performance of RED systems, including power density, efficiency and long-term stability, strongly relies on the physical/chemical properties of IEM, such as membrane resistance, antifouling ability, and chemical stability, which calls for significant advances in membrane fabrication technology [15–18].

Different approaches have been tried to improve the IEM-based RED performance, including using membrane stacks [10], developing novel electrode systems [19–22], and optimizing cell parameters, such as spacer thickness [23–25], inter-membrane distance [17, 26, 27], solution composition [6, 7, 27], and flow velocity [10, 23, 28]. Alternative RED systems have also been explored for energy harvesting, among which nanofluidics has attracted great attention recently. Benefitting from the intrinsic property of ion-selectivity induced by the overlap of electrical double layers (EDLs) in nanostructures, nanofluidic channels function like ion exchange membranes [29–31]. Guo *et al* [32, 33] explored this scheme by establishing an ionic concentration gradient across cation-selective nanochannels (or nanopores), so that more cations diffuse through the nanochannels than anions do, thereby forming an electrical current across the nanochannels, namely nanofluidic reverse electrodialysis (NRED). They obtained a maximum single nanopore output power of $\sim 26 \text{ pW}$ (power density of $\sim 8.3 \text{ W m}^{-2}$) and a maximum efficiency of $\sim 4\%$ in track-etched conical nanochannels with base and tip diameters of $1\text{--}2 \mu\text{m}$ and 41 nm , respectively, in a $12 \mu\text{m}$ thick polyimide film. However, as is the problem with IEMs, organic membranes lack reliability for long-term and complicated real applications since they may shrink and swell in response to the environment [34]. By using 4 nm high silica nanochannels as the key ion-selective structure, Kim *et al* [35, 36] obtained a power density of 7.7 W m^{-2} along with an efficiency of 31%, of which the total output power was on the order of picowatts. Despite the improvement in power density of the NRED scheme, there are practical limitations: integration of adequate nanochannels in one single chip for devices with power requirement higher than nanowatts is

not only technically challenging, but also expensive and time-consuming.

To overcome the scaling-up problem, we proposed a nanofluidic crystal (NFC) based scaling-up scheme for NRED that is promising for constructing a facile, high-efficiency, and high-power-density energy harvester with high output power. Unlike nanochannels prepared by top-down nanofabrication techniques or nanoporous materials synthesized by bottom-up methods, the NFC is easily obtained from self-assembly of monodispersed nanoparticles in predefined microstructures. Although the NFC has been extensively studied as a photonic bandgap structure [37, 38], sphere-lithography masks [39, 40], templates for macroporous materials fabrication [41], and optical sensors [42], little attention has been paid to its potential applications as a nanofluidic material. Our previous works have demonstrated both experimentally and theoretically that NFC inside a microchannel [43] or suspended in a micropore [44, 45] exhibits the typical electrokinetics properties of an individual nanochannel but with an enlarged effective cross-sectional area. The interstices of the NFC can be equivalent to a nanofluidic network with numerous nanochannels in parallel, and thereby has the potential to provide a large electrical output in NRED energy harvesting systems. In this paper, as a proof-of-concept demonstration of the scaling-up capability of NFC, we study the energy harvesting performance of a NFC-based NRED prototype cell and its temporal behavior.

2. Experiment

2.1. Working principle

The isoelectric point of silica is around 2 [46]. Below the isoelectric point, silanol groups get protonated and above it they get deprotonated, exhibiting positive and negative charges respectively. In the solution with pH of ~ 5.6 (carbon dioxide saturated water) used in our experiment, silica nanoparticles with hydroxyl groups on the surface exhibited negatively charged surface. According to our previous work [43], the surface charge density of nanoparticles used here was around $1.8 \times 10^{-2} \text{ C m}^{-2}$. The negatively charged nanoparticles attract cations and repel anions, which causes positively charged EDLs to form near the surfaces. The characteristic thickness of the EDL can be estimated by the well-known Debye length, λ_D , which is inversely proportional to the square root of the ionic concentration of the buffer [47].

When interstices in the NFC have sizes comparable to the Debye length, EDLs will be overlapped. Therefore, the nanochannel network of the NFC will possess a character of cation-selectivity, usually quantified by the transference number, t_+ , defined as the fraction of total current carried by the dominant ions [48], cations in this case. When a concentration gradient is applied across the cation-selective NFC, which functions as an IEM, more cations diffuse from the concentrated side (c_H) to the dilute one (c_L) than anions do, as shown in figure 1. Therefore, the Donnan potentials developed at both ends of the NFC, plus the electrical potential inside the NFC due to diffusion [47], constitutes an

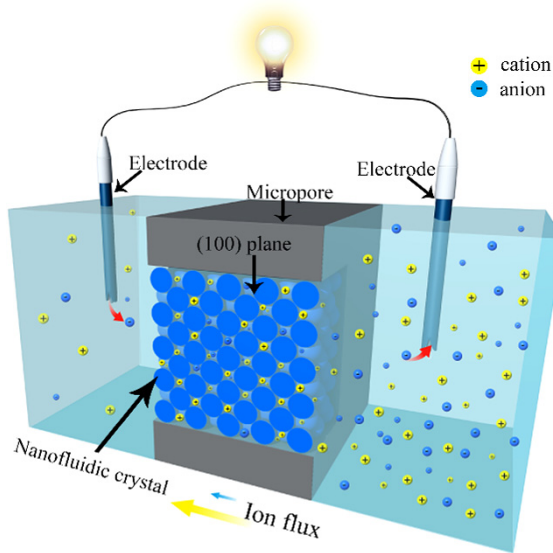


Figure 1. Schematic illustration of energy harvesting by nanofluidic reverse electrodialysis from concentration gradient across a nanofluidic crystal (NFC). When a concentration gradient is applied across a cation-selective NFC, more cations diffuse through the NFC than anions do. An electrical potential drop along the net ion diffusion is established. The Gibbs free energy that drives ion diffusion is thus converted into electricity.

electrical potential drop along the net ion diffusion, namely the diffusion potential E_{diff} , which can be calculated as [35]

$$E_{\text{diff}} = (2t_+ - 1) \frac{RT}{zF} \ln \frac{\gamma_{\text{CH}} c_{\text{H}}}{\gamma_{\text{CL}} c_{\text{L}}}, \quad (1)$$

where R , T , z , F , γ represent the gas constant, temperature, ion valence, Faraday constant, and mean activity coefficient, respectively. The Gibbs free energy, which drives this ion diffusion, is thus converted into electricity, i.e. harvesting energy based on the NRED principle.

2.2. Nanofluidic crystal preparation

To realize the NFC used in the present work, a micropore ($40 \times 40 \mu\text{m}^2$) through a suspended silicon membrane ($50 \mu\text{m}$ thick) was fabricated by the standard silicon microfabrication process, introduced in [45]. Monodispersed silica nanoparticles with diameters of 100/210/500 nm and hydroxyl groups on the surface (Technical Institute of Physics and Chemistry of Chinese Academic Society, P R China, see appendix A for details) were then loaded into the micropore. When ethanol, the base fluid of the nanoparticle suspension, was evaporated slowly under a controlled condition, silica nanoparticles were self-assembled into a face-centered cubic (fcc) crystalline structure, as shown in figure 2(a), which was the NFC ready for the energy harvesting test. The whole process of nanofluidic crystal self-assembly was finished within 30 min.

2.3. Structure of the prototype cell

In this work, in order to directly evaluate the performance of NFC for NRED energy harvesting, we designed a

simplified prototype cell, as shown in figure 2(b). Two potassium chloride solutions with different concentrations were separately loaded in two PMMA reservoirs ($1.5 \times 1.5 \times 2 \text{ cm}^3$, 4.5 ml). A silicon chip with the NFC packed in a micropore bridged the two reservoirs with O-rings for leakage-proofing. The electrodes used in our experiment were Ag/AgCl electrodes (Shanghai Chenhua Instrument Co. Ltd, CHI111).

2.4. Characterization of the prototype cell

To characterize the energy harvesting performance of the prototype cell, I - V testing was performed by applying an external voltage, E_{source} , with a precision semiconductor parameter analyzer HP4156B. The Ag/AgCl electrodes were connected to HP4156B through an accessorial Faraday Cage (figure 2(b)). During the I - V test, the high concentration side was grounded, and the potential of the low concentration side varied linearly from 0 to 250 mV, with a step of 10 mV. Each I - V test lasted about 1 min.

Due to the redox reactions, there were additional potential drops at the interfaces between the Ag/AgCl electrodes and the KCl solutions, i.e. $E_{\text{electrode}, c_{\text{L}}}$ (low concentration side) and $E_{\text{electrode}, c_{\text{H}}}$ (high concentration side). The presence of a concentration gradient resulted in unequal potential drops at two electrodes, constituting the overall electrode potential, $E_{\text{electrode}}$, which was the difference of $E_{\text{electrode}, c_{\text{L}}}$ and $E_{\text{electrode}, c_{\text{H}}}$. $E_{\text{electrode}}$ was measured in advance. Figure 2(c) is the equivalent circuit of the testing system, where E_{diff} and r represent the open circuit voltage and internal resistance of the prototype cell, respectively. The parasitic resistances, R_{para} , including the internal resistance of voltage source, the serial resistance of the wiring, the resistance at the interfaces of electrodes and the electrolyte, and bulk solution resistances, were negligible compared to r (see supplementary information for more details available at stacks.iop.org/Nano/24/345401/mmedia). E_{diff} and r were extracted from the measured I - V curve by using the following relationship:

$$I = \frac{1}{r} E_{\text{source}} - \frac{1}{r} (E_{\text{electrode}} + E_{\text{diff}}). \quad (2)$$

Figure 2(d) shows a typical I - V curve of the prototype cell, which exhibited perfect Ohmic conducting behavior. The energy harvesting performances of NFCs with three different nanoparticle diameters were measured at varied concentration gradients. The low concentration, c_{L} , was fixed at 0.1 mM ($\lambda_{\text{D}} = 30.5 \text{ nm}$) while the high concentration (c_{H}) varied from 0.3 mM ($\lambda_{\text{D}} = 17.6 \text{ nm}$), 1 mM ($\lambda_{\text{D}} = 9.6 \text{ nm}$), 3 mM ($\lambda_{\text{D}} = 5.6 \text{ nm}$), 10 mM ($\lambda_{\text{D}} = 3.1 \text{ nm}$), 30 mM ($\lambda_{\text{D}} = 1.8 \text{ nm}$), to 100 mM ($\lambda_{\text{D}} = 1.0 \text{ nm}$).

2.5. Electrode calibration

Due to the redox reactions at the interfaces between Ag/AgCl electrodes and KCl solutions, there exists an additional electrode potential drop, $E_{\text{electrode}}$, which varies

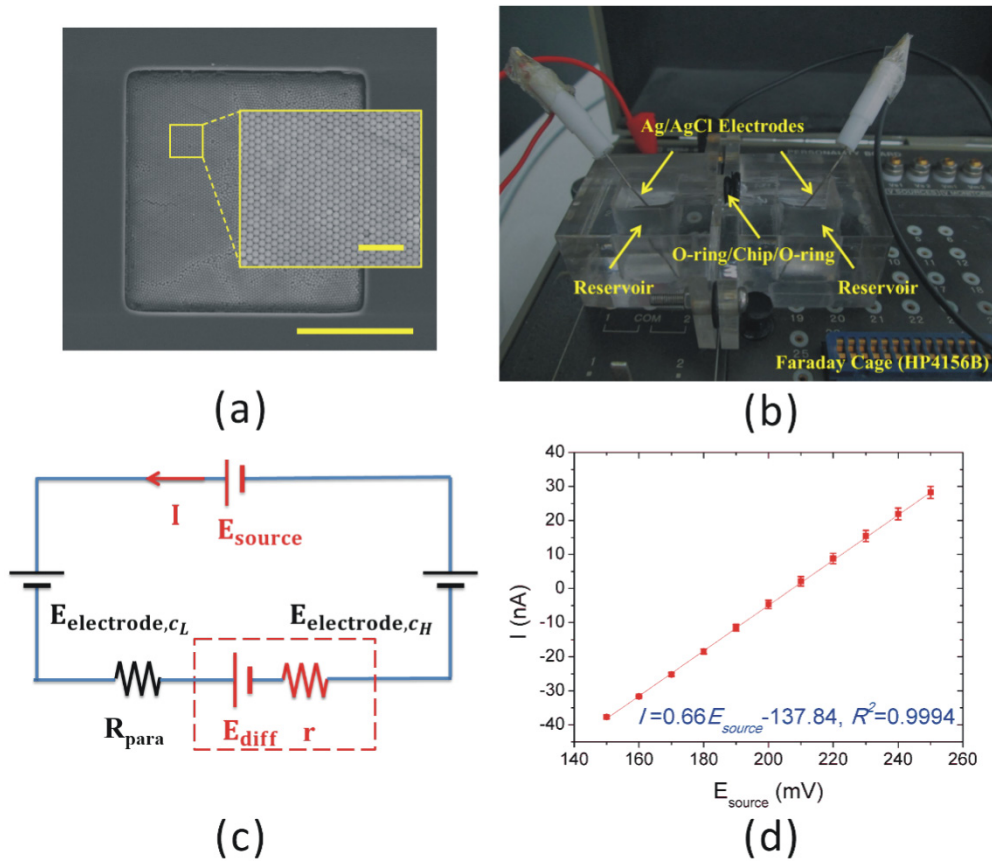


Figure 2. Structure of the prototype cell and I - V characterization. (a) SEM photos of NFC with nanoparticle diameter of 500 nm packed in a $40 \times 40 \mu\text{m}^2$ micropore. The scale bar is $20 \mu\text{m}$ ($3 \mu\text{m}$ in the inserted photo). (b) Experimental setup. (c) Equivalent circuit diagram. (d) Typical I - V curve. I - V curve of the prototype cell with nanoparticle diameter of 210 nm at 0.1 mM|100 mM.

with the concentration of the KCl solution. $E_{electrode}$ can be theoretically predicted by the Nernst equation [49],

$$E_{electrode} = \frac{RT}{zF} \ln \frac{\gamma_{CH} c_H}{\gamma_{CL} c_L}. \quad (3)$$

In order to extract the diffusion potential E_{diff} from equation (2), we have to measure the electrode potential $E_{electrode}$ in advance. The setup of the electrode calibration experiment was the same as that of the I - V test of the prototype cell, except that the silicon chip used here was not packed with nanoparticles. Ions diffused from the high-concentration KCl solution to the low one through the non-ion-selective micropore. Because the ionic current (<100 nA) through the micropore did not affect the bulk concentration observably in the first several minutes, the electrode potential remained stable during the calibration. The experimental and theoretical electrode potential is compared in table 1. The experimental values in general fit with the theoretical values. We used these measured data for calculating the diffusion potential E_{diff} .

2.6. Stability test of the prototype cell

In order to estimate the stability of prototype cell as a power source, we performed I - V test of the prototype cell every 5 min in 3 h using the experimental setup shown in figure 2(b).

The NFC used here was obtained by packing nanoparticles with diameter of 100 nm in a $100 \times 100 \mu\text{m}^2$ micropore. The concentration gradient was 10 mM|0.1 mM, at which the prototype cell demonstrated the largest open circuit voltage.

3. Results and discussions

3.1. I - V characteristics

As shown in figure 3(a), NFCs with smaller nanoparticle diameters exhibited higher open circuit voltages at the same concentration gradient. NFC constructed by nanoparticles with smaller diameter had smaller interstices, thereby higher ion-selectivity, which resulted in a larger open circuit voltage, as indicated by equation (1). For the same NFCs with nanoparticle diameter of 100/210/500 nm, with the concentration gradient increasing, the open circuit voltage reached maximum values of $91.39 \pm 0.49/74.12 \pm 1.40/19.42 \pm 0.49$ mV, respectively, and then dropped to different extents. On the one hand, an increased c_H gave a larger Gibbs free energy driving the ions to diffuse across the NFC, thereby tending to increase the potential drop.

On the other hand, the Debye length of interstices near the high-concentration side decreased dramatically with the bulk concentration increasing, which led to degradation of the ion-selectivity considerably. t_+ , the indicator of the

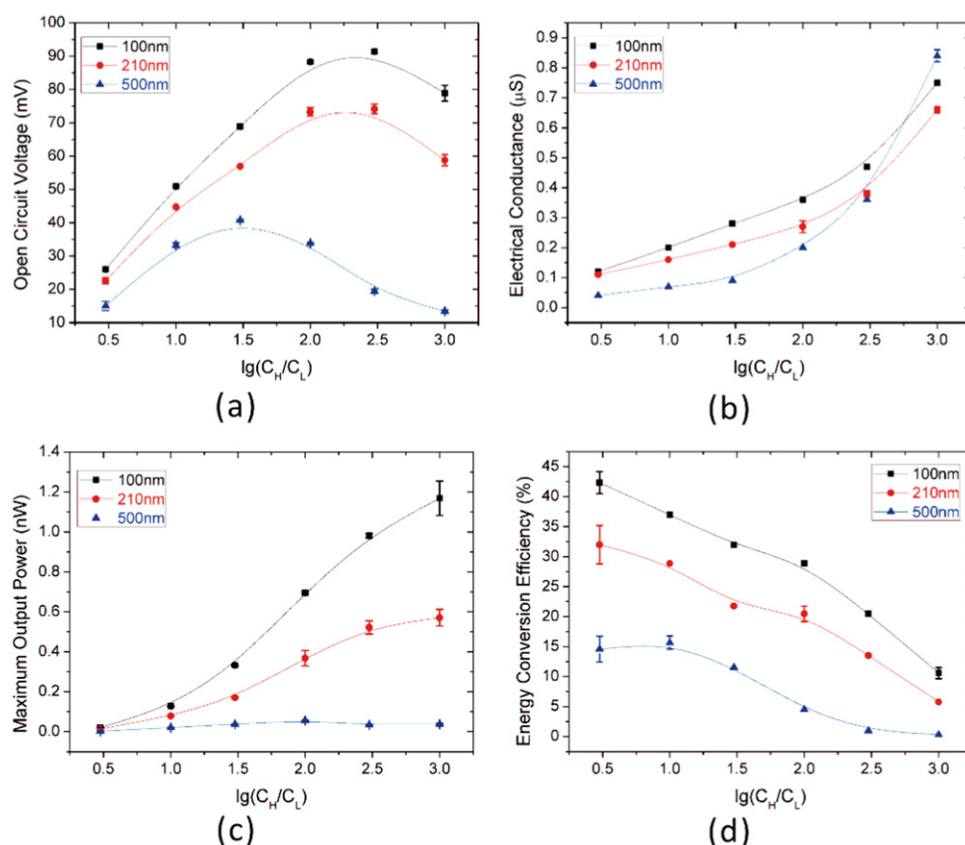


Figure 3. Performances of the prototype cell. (a) Open circuit voltage. (b) Electrical conductance. (c) Maximum output power. (d) Energy conversion efficiency.

Table 1. Comparison between the experimental and theoretical electrode potential.

	0.1 mM 0.3 mM	0.1 mM 1.0 mM	0.1 mM 3.0 mM	0.1 mM 10 mM	0.1 mM 30 mM	0.1 mM 100 mM
Theoretical estimation (mV)	28.0	58.6	86.2	116.0	142.6	171.2
Experimental measurement (mV)	27.5	51.5	77.8	105.9	127.4	150.6

Table 2. Transference numbers, t_+ , in the present work.

Nanoparticle diameter (nm)	0.1 mM 0.3 mM	0.1 mM 1.0 mM	0.1 mM 3.0 mM	0.1 mM 10 mM	0.1 mM 30 mM	0.1 mM 100 mM
100	0.96 ± 0.01	0.93	0.90	0.88	0.82	0.73 ± 0.01
210	0.90 ± 0.02	0.88	0.83	0.82 ± 0.01	0.76	0.67
500	0.77 ± 0.02	0.78 ± 0.01	0.74	0.65	0.57	0.54

ion-selectivity, was calculated from equation (1) and values are listed in table 2. These counter-effects determined the optimized E_{diff} shown in figure 3(a).

Figure 3(b) shows the conductance of the NFC-based NRED prototype cell at different concentration gradients. As mobile ions in the EDL follow the Boltzmann distribution [47], counter-ion concentration decays exponentially from charged surfaces. Therefore, NFCs with smaller nanoparticle diameters, i.e. with smaller equivalent nanochannel size, have larger counter-ion concentration in the interstices and demonstrate larger conductivity. Meanwhile,

for any ideally close-packed nanoparticle crystal, the space occupation rate (74.05%) is independent of the nanoparticle diameter, which means that the effective nanochannel volume is the same for NFCs packed in micropores of identical size. Therefore, NFCs with smaller nanoparticle diameters that exhibit larger conductivity also exhibit larger conductance. The conductance of the NFC consisted of two parts: (1) conductance of bulk solution outside the EDL, which was proportional to ion concentration, (2) conductance contributed by counter-ions in the EDL which was dependent on surface charge density of nanoparticles. With the bulk concentration

Table 3. Performance comparison of different RED energy harvesting systems.

	Ion exchange membrane based RED systems				Nanofluidic RED systems		
	Large-scale		Micro-scale		Nano-scale	Micro/nano-scale	
Authors	Turek <i>et al</i> [7]	Veerman <i>et al</i> [10]	Sadeghian <i>et al</i> [13]	Sales <i>et al</i> [14]	Guo <i>et al</i> [32]	Kim <i>et al</i> [35]	Present study
Structure	10 pairs stack	50 cells stack	Single stage	8 cells stack	Single stage	Single stage	Single stage
Power (pW)	—	9.3×10^{10}	—	—	26	~1	1170 ± 90
Power density (W m^{-2})	0.46	0.95	0.0002	0.072	~8.3	7.7	2.82 ± 0.22
Efficiency (%)	—	18	0.44	22	4	31	42.32 ± 1.84
Scalability	High	High	High	High	Medium	Low	High
Material	Organic	Organic	Organic	Organic	Organic	Inorganic	Inorganic

increasing, the EDL thickness decreased and the bulk concentration played a more important role in determining the conductance of NFC. As a result, the conductance of NFC increased with bulk concentration. NFC with nanoparticle diameter of 500 nm showed larger conductance at 0.1 mM|100 mM, which can probably be attributed to bulk concentration variation caused by ion diffusion. Ion diffusion from the high-concentration side increases the bulk concentration at the low-concentration side, which consequently increases the conductance of the NFC. This was most obvious in the 500 nm sample, because it had the largest equivalent nanochannel size and therefore its conductance showed stronger dependence on bulk concentration.

For any ideally close-packed nanoparticle crystal, the effective cross-sectional area S_{eff} can be expressed as $S_{\text{eff}} = 0.2595S_m$ where S_m represents the cross-sectional area of the micropore. Therefore, unlike in regular nanochannels where there was a tradeoff between the ion-selectivity and the effective cross-sectional area, the NFC had the unique advantage that its effective cross-sectional area was insensitive to the particle diameter, which meant that it was possible to pursue higher ion-selectivity by using much smaller nanoparticles. Thanks to the large effective cross-sectional area of the NFC and enormous surface-to-volume ratio, the electrical conductance was about three orders of magnitude larger than reported for the energy harvesting system based on silica nanochannels (~1 nS) [35].

It is well known that the maximum output power of an energy harvesting system is obtained when the load resistance R_L is equal to the internal one, i.e. $R_L = r$. For the present prototype cell

$$P_{\text{max}} = \frac{E_{\text{diff}}^2}{4r}. \quad (4)$$

P_{max} is calculated based on the values of E_{diff} and r (reciprocal of conductance) shown in figures 3(a) and (b), and plotted in figure 3(c). Since NFCs with a nanoparticle diameter of 100 nm demonstrated both the highest open circuit voltage and the largest electrical conductance at the same concentration gradient, their maximum output power also stood out as the best and reached 1.17 ± 0.09 nW at 0.1 mM|100 mM within the present experiments. Therefore, the largest output power density in this work was 2.82 ± 0.22 W m⁻². The efficiency corresponding to the maximum

power was given as $\eta_{\text{max}} = (2t_+ - 1)^2/2$ [32, 35], with a theoretical maximum efficiency of 50%. As shown in figure 3(d), the maximum efficiency obtained here was $42.32 \pm 1.84\%$ at a concentration gradient of 0.1 mM|0.3 mM in NFCs with the nanoparticle diameter of 100 nm.

In table 3, we compare the performance of different RED energy harvesting systems. Compared to micro-scale IEM-based RED systems [13, 14], the present work demonstrates high efficiency and high power density. Compared to track-etched nanochannels in PET membrane [32], the present work demonstrates high efficiency and good environmental compatibility. While maintaining the advantages of high efficiency, high power density and good environmental compatibility in silica nanochannels [35], the present work shows good scaling-up capability.

3.2. Stability

With ions in the high-concentration solution diffusing to the low-concentration solution through the 100×100 μm^2 micropore packed with NFC, the concentration gradient between the two ends of the NFC might decrease and consequently the performance of the prototype cell as a power source might degrade.

The characteristic diffusion distance W can be estimated as

$$W \sim 2\sqrt{Dt_1}, \quad (5)$$

where D and t_1 represent ion diffusivity and diffusion time, respectively. In this case, the diffusivities of K^+ and Cl^- , D , were taken as the typical value for ions, 2.0×10^{-9} m² s⁻¹, and $t_1 = 3$ h. The diffusion distance W calculated was 0.93 cm, which is much smaller than the distance between the electrodes and the chip (2.5 cm). Therefore the electrode potential $E_{\text{electrode}}$ remained stable during the experiment, which was also confirmed by a 1D simulation (see appendix B for details).

As shown in figure 4(a), the short circuit current, I_{sc} gradually increased with time at a decreasing slope. The quantity of cations transported to the low-concentration solution can be estimated by the following formula:

$$n_{\text{K}^+} = \frac{t_+}{2t_+ - 1} \frac{1}{eN_A} \int_0^{t_1} I_{\text{sc}}(t) dt, \quad (6)$$

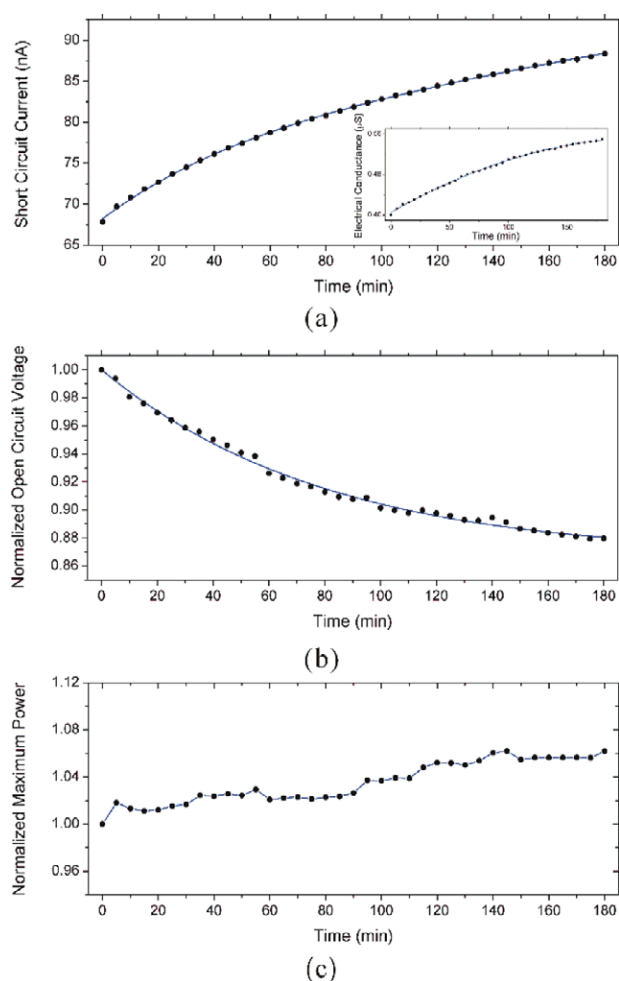


Figure 4. Stability of the prototype cell. (a) Short circuit current, the inset is the electrical conductance variation with time. (b) Normalized open circuit voltage. The open circuit voltage was normalized by being divided by the open circuit voltage at $t = 0$. (c) Normalized maximum power. The maximum power was normalized by being divided by the maximum power at $t = 0$.

where the elementary charge $e = 1.60 \times 10^{-19}$ C, Avogadro's number $N_A = 6.021\,023 \text{ mol}^{-1}$, and $I_{sc}(t)$ was the fitted curve of I_{sc} . In the stability test, the transference number $t_+ \approx 0.8$ and the diffusion time $t_1 = 3 \text{ h}$, so according to equation (6), the quantity of cations transported to the low-concentration solution was $1.28 \times 10^{-8} \text{ mol}$. Due to the limited diffusivities, ions accumulated near the NFC, leading to the increase of concentration at the low-concentration end of the NFC. Meanwhile, the bulk concentration increment weakened the dominance of EDLs on the conductance of NFC. Consequently, the conductance of NFC increased with the bulk concentration, as indicated by figure 4(a) inset.

The decrease of concentration gradient also resulted in decrease of the open circuit voltage as shown in figure 4(b). The open circuit voltage dropped to 88% of the initial value after 3 h. As indicated by equation (4), the counter-effect of increasing conductance and decreasing open circuit voltage determined the variation of maximum power. In this experiment, the maximum power remained relatively stable, with a slight increment to 107% of the initial value.

It is worth mentioning that in the present work, ion solutions were kept static in the two reservoirs. One potential issue to be addressed is how to keep constant concentrations on both ends of the NFC. For applications where there is a bulk solution flow, such as blood flow, the diffusion-induced concentration variation would be compensated by the flowing solution, thereby maintain the concentration gradient and energy harvesting performance as well.

4. Conclusion

With a proof-of-concept prototype cell, we have demonstrated a NFC-based scaling-up scheme that is promising for constructing a facile, high-efficiency and high-power-density energy harvester with high output power based on the NRED principle. The kernel NFC for a single device was prepared within 30 min, and provided a maximum efficiency of $42.3 \pm 1.84\%$, a maximum power density of $2.82 \pm 0.22 \text{ W m}^{-2}$, and a maximum output power amplification of nearly three orders of magnitude ($1.17 \pm 0.09 \text{ nW/unit}$) in the present experiment. The output power can be further improved by using nanoparticles with smaller diameters and higher surface charge densities, which are already off-the-shelf. The open circuit voltage had a decrement of 12% and the output power increased 7% during a 3-h test. By exploiting parallelization and cascade, we can scale up the current NFC-based NRED prototype cell to achieve desired output powers and open circuit voltages for practical applications. This scheme has the potential of utilizing ionic concentration gradient ubiquitously existing in nature or in human body, for building self-powered micro/nano-scale systems.

Acknowledgments

This work was financially supported by the Major State Basic Research Development Program (973 Program) (Grant Nos 2009CB320300 and 2011CB309502) and the National Natural Science Foundation of China (Grant Nos 60976086 and 91023045).

Appendix A. Synthesis of monodispersed silica nanoparticles

The monodispersed silica nanoparticles used in the experiment are synthesized by the widely adopted Stöber process. Water, ethanol and ammonia with certain volume ratio are first added into a reaction kettle and homogeneously mixed. Then, tetraethyl orthosilicate (TEOS) is added to the mixture. The reactions taking place are hydrolysis of the silyl ether to a silanol followed by condensation reactions. Monodispersed silica nanoparticle suspension is obtained from the nucleation of hydrolyzates after several hours' reaction. The silica nanoparticles synthesized by this process contain hydroxyl groups on the surface. The price of the above-mentioned nanoparticles was 800 RMB/10 ml, so the cost of nanofluidic crystal for each device (a volume of $3 \mu\text{l}$ was used) was $3 \mu\text{l}/10 \text{ ml} \times 800 \text{ RMB} = 0.24 \text{ RMB}$, which equaled 0.038 USD.

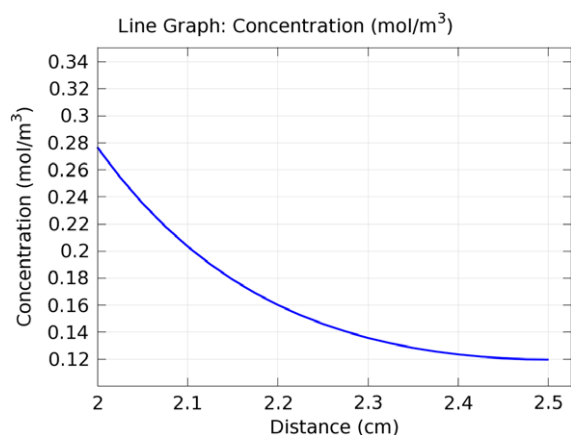


Figure B.1. 1D simulation of the reservoir concentration variation.

Appendix B. 1D simulation of the reservoir end concentration variation

A 1D transient simulation was performed using COMSOL Multiphysics 4.2. The studied dimension was 2.5 cm (from the chip to the end of the reservoir where the electrode was placed). The boundary conditions were: on one chip end, there was a constant inward flux f , which represents the ion diffusion flux from the NFC; on the reservoir end, there was no flux in or out since the reservoir is closed. f was calculated as

$$f = \frac{I_{sc}}{eN_A S}, \quad (\text{B.1})$$

where I_{sc} , e , N_A , S represent the short circuit current, elementary charge, Avogadro's number, and micropore area. The short circuit current I_{sc} was taken as 100 nA and the micropore area S was $1 \times 10^{-8} \text{ m}^2$ in this case. According to equation (B.1), f was $1 \times 10^{-4} \text{ mol m}^{-2} \text{ s}^{-1}$. The initial concentration was set at 0.1 mM, and the simulation time was 3 h. As shown in figure B.1, at the end of the reservoir where the electrode was placed, the concentration increased from 0.1 to 0.12 mM. It is worth mentioning that in a real prototype cell, the variation would be much lower since the 1D model neglects the actual volume of the bulk concentration.

References

- [1] Wang Z L 2008 Self-powered nanotech—nanosize machines need still tinier power plants *Sci. Am.* **298** 84–7
- [2] Shankar K, Mor G K, Prakasam H E, Yoriya S, Paulose M, Varghese O K and Grimes C A 2007 Highly-ordered TiO_2 nanotube arrays up to 220 μm in length: use in water photoelectrolysis and dye-sensitized solar cells *Nanotechnology* **18** 065707
- [3] Cuadras A, Gasulla M and Ferrari V 2010 Thermal energy harvesting through pyroelectricity *Sensors Actuators A* **158** 132–9
- [4] Beeby S P, Torah R N, Tudor M J, Glynne-Jones P, O'Donnell T, Saha C R and Roy S 2007 A micro electromagnetic generator for vibration energy harvesting *J. Micromech. Microeng.* **17** 1257–65
- [5] Pattle R E 1954 Production of electric power by mixing fresh and salt water in the hydroelectric pile *Nature* **174** 660
- [6] Weinstein J N and Leitz F B 1976 Electric-power from difference in salinity—dialytic battery *Science* **191** 557–9
- [7] Turek M and Bandura B 2007 Renewable energy by reverse electrodialysis *Desalination* **205** 67–74
- [8] Suda F, Matsuo T and Ushioda D 2007 Transient changes in the power output from the concentration difference cell (dialytic battery) between seawater and river water *Energy* **32** 165–73
- [9] Post J W, Hamelers H V M and Buisman C J N 2008 Energy recovery from controlled mixing salt and fresh water with a reverse electrodialysis system *Environ. Sci. Technol.* **42** 5785–90
- [10] Veerman J, Saakes M, Metz S J and Harmsen G J 2009 Reverse electrodialysis: performance of a stack with 50 cells on the mixing of sea and river water *J. Membr. Sci.* **327** 136–44
- [11] Vermaas D A, Saakes M and Nijmeijer K 2011 Doubled power density from salinity gradients at reduced intermembrane distance *Environ. Sci. Technol.* **45** 7089–95
- [12] Vermaas D A, Guler E, Saakes M and Nijmeijer K 2012 Theoretical power density from salinity gradients using reverse electrodialysis *Energy Procedia* **20** 170–84
- [13] Sadeghian R B, Pantchenko O, Tate D and Shakouri A 2011 Miniaturized concentration cells for small-scale energy harvesting based on reverse electrodialysis *Appl. Phys. Lett.* **99** 173702
- [14] Sales B B, Saakes M, Post J W, Buisman C J N, Biesheuvel P M and Hamelers H V M 2010 Direct power production from a water salinity difference in a membrane-modified supercapacitor flow cell *Environ. Sci. Technol.* **44** 5661–5
- [15] Lacey R E 1980 Energy by reverse electrodialysis *Ocean. Eng.* **7** 1–47
- [16] Vermaas D A, Kunteng D, Saakes M and Nijmeijer K 2012 Fouling in reverse electrodialysis under natural conditions *Water Res.* **47** 1289–98
- [17] Dlugolecki P, Nijmeijer K, Metz S and Wessling M 2008 Current status of ion exchange membranes for power generation from salinity gradients *J. Membr. Sci.* **319** 214–22
- [18] Xu T W 2005 Ion exchange membranes: state of their development and perspective *J. Membr. Sci.* **263** 1–29
- [19] Veerman J, Saakes M, Metz S J and Harmsen G J 2010 Reverse electrodialysis: evaluation of suitable electrode systems *J. Appl. Electrochem.* **40** 1461–74
- [20] Burheim O S, Seland F, Pharoah J G and Kjølstrup S 2012 Improved electrode systems for reverse electro-dialysis and electro-dialysis *Desalination* **285** 147–52
- [21] Vermaas D A, Bajracharya S, Sales B B, Saakes M, Hamelers B and Nijmeijer K 2013 Clean energy generation using capacitive electrodes in reverse electrodialysis *Energy Environ. Sci.* **6** 643–51
- [22] Rica R A, Brogioli D, Ziano R, Salerno D and Mantegazza F 2012 Ions transport and adsorption mechanisms in porous electrodes during capacitive-mixing double layer expansion (CDLE) *J. Phys. Chem. C* **116** 16934–8
- [23] Veerman J, Saakes M, Metz S J and Harmsen G J 2010 Electrical power from sea and river water by reverse electrodialysis: a first step from the laboratory to a real power plant *Environ. Sci. Technol.* **44** 9207–12
- [24] Veerman J, Saakes M, Metz S J and Harmsen G J 2011 Reverse electrodialysis: a validated process model for design and optimization *Chem. Eng. J.* **166** 256–68
- [25] Dlugolecki P, Dabrowska J, Nijmeijer K and Wessling M 2010 Ion conductive spacers for increased power generation in reverse electrodialysis *J. Membr. Sci.* **347** 101–7
- [26] Dlugolecki P, Gambier A, Nijmeijer K and Wessling M 2009 Practical potential of reverse electrodialysis as process for sustainable energy generation *Environ. Sci. Technol.* **43** 6888–94

- [27] Brauns E 2009 Salinity gradient power by reverse electrodialysis: effect of model parameters on electrical power output *Desalination* **237** 378–91
- [28] Veerman J, de Jong R M, Saakes M, Metz S J and Harmsen G J 2009 Reverse electrodialysis: comparison of six commercial membrane pairs on the thermodynamic efficiency and power density *J. Membr. Sci.* **343** 7–15
- [29] Pennathur S, Eijkel J C T and van den Berg A 2007 Energy conversion in microsystems: is there a role for micro/nanofluidics? *Lab Chip* **7** 1234–7
- [30] Meng D and Allen J 2008 Micro- and nanofluidics for energy conversion *IEEE Nanotechnol. Mag.* **2** 19–23
- [31] Yang Y and Jing L 2011 Micro/nanofluidics-enabled energy conversion and its implemented devices *Front. Energy* **5** 270–87
- [32] Guo W, Cao L, Xia J, Nie F-Q, Ma W, Xue J, Song Y, Zhu D, Wang Y and Jiang L 2010 Energy harvesting with single-ion-selective nanopores: a concentration-gradient-driven nanofluidic power source *Adv. Funct. Mater.* **20** 1339–44
- [33] Cao L, Guo W, Ma W, Wang L, Xia F, Wang S, Wang Y, Jiang L and Zhu D 2011 Towards understanding the nanofluidic reverse electrodialysis system: well matched charge selectivity and ionic composition *Energy Environ. Sci.* **4** 2259–66
- [34] Chu K-L, Shannon M A and Masel R I 2006 An improved miniature direct formic acid fuel cell based on nanoporous silicon for portable power generation *J. Electrochem. Soc.* **153** A1562
- [35] Kim D-K, Duan C, Chen Y-F and Majumdar A 2010 Power generation from concentration gradient by reverse electrodialysis in ion-selective nanochannels *Microfluid. Nanofluid.* **9** 1215–24
- [36] Kim D-K 2011 Numerical study of power generation by reverse electrodialysis in ion-selective nanochannels *J. Mech. Sci. Technol.* **25** 5–10
- [37] Huang C-K, Chan C-H, Chen C-Y, Tsai Y-L, Chen C-C, Han J-L and Hsieh K-H 2007 Rapid fabrication of 2D and 3D photonic crystals and their inversed structures *Nanotechnology* **18** 265305
- [38] Yong V, Aagesen L K and Chang R P H 2008 Growth of highly ordered colloidal photonic crystals using a modeling approach *Nanotechnology* **19** 435204
- [39] Brown E C, Wilke S K, Boyd D A, Goodwin D G and Haile S M 2010 Polymer sphere lithography for solid oxide fuel cells: a route to functional, well-defined electrode structures *J. Mater. Chem.* **20** 2190–6
- [40] Zhang J, Li Y, Zhang X and Yang B 2010 Colloidal self-assembly meets nanofabrication: from two-dimensional colloidal crystals to nanostructure arrays *Adv. Mater.* **22** 4249–69
- [41] Kurdyukov D A, Feoktistov N A, Nashchekin A V, Zadiranov Y M, Aleksenskii A E, Ya Vul' A and Golubev V G 2012 Ordered porous diamond films fabricated by colloidal crystal templating *Nanotechnology* **23** 015601
- [42] Yang H, Jiang P and Jiang B 2012 Vapor detection enabled by self-assembled colloidal photonic crystals *J. Colloid Interface Sci.* **370** 11–8
- [43] Chen Z, Wang Y, Wang W and Li Z 2009 Nanofluidic electrokinetics in nanoparticle crystal *Appl. Phys. Lett.* **95** 102105
- [44] Lei Y, Wang W, Wu W and Li Z 2010 Nanofluidic diode in a suspended nanoparticle crystal *Appl. Phys. Lett.* **96** 263102
- [45] Lei Y, Xie F, Wang W, Wu W and Li Z 2010 Suspended nanoparticle crystal (S-NPC): a nanofluidics-based, electrical read-out biosensor *Lab Chip* **10** 2338–40
- [46] Parks G A 1965 The isoelectric points of solid oxides, solid hydroxides, and aqueous hydroxo complex systems *Chem. Rev.* **65** 177–98
- [47] Schoch R, Han J and Renaud P 2008 Transport phenomena in nanofluidics *Rev. Mod. Phys.* **80** 839–83
- [48] Cervera J, Alcaraz A, Schiedt B, Neumann R and Ramirez P 2007 Asymmetric selectivity of synthetic conical nanopores probed by reversal potential measurements *J. Phys. Chem. C* **111** 12265–73
- [49] Bard A J and Faulkner L R 1980 *Electrochemical Methods: Fundamentals and Applications* vol 2 (New York: Wiley)